Accepted Manuscript

Efficient fast Fourier transform-based numerical implementation to simulate large strain behavior of polycrystalline materials

Jaspreet S. Nagra, Abhijit Brahme, Ricardo A. Lebensohn, Kaan Inal

PII: S0749-6419(17)30138-9

DOI: 10.1016/j.ijplas.2017.07.001

Reference: INTPLA 2220

To appear in: *International Journal of Plasticity*

Received Date: 21 March 2017

Revised Date: 26 June 2017

Accepted Date: 2 July 2017

Please cite this article as: Nagra, J.S., Brahme, A., Lebensohn, R.A., Inal, K., Efficient fast Fourier transform-based numerical implementation to simulate large strain behavior of polycrystalline materials, *International Journal of Plasticity* (2017), doi: 10.1016/j.ijplas.2017.07.001.

Efficient Fast Fourier Transform-based Numerical Implementation to Simulate Large Strain Behavior of Polycrystalline Materials

Jaspreet S. Nagra[1], Abhijit Brahme[1], Ricardo A. Lebensohn[2], Kaan Inal[1]

[1]University of Waterloo, 200 University Ave. West, Waterloo, ON N2L 3G1, Canada
[2] Los Alamos National Laboratory, MS G755, Los Alamos, NM 87845, USA

Abstract

In this paper, a new full-field numerical framework is proposed to model large strain phenomena in polycrystals. The proposed framework is based on the elasto-viscoplastic (EVP) fast Fourier transform (FFT) formulation presented by Lebensohn et al. (2012) and the rate dependent crystal plasticity framework developed by Asaro and Needleman (1985). In this implementation, the full-field solutions of micromechanical fields are computed on a regular, voxelized representative volume element (RVE) in which either a single or multiple grid points represent a single grain. The Asaro and Needleman (1985) formulation coupled with a semi-explicit, forward gradient time-integration scheme (Peirce et al., 1983) is used to compute local stresses and the FFT-based method is used to find local strain fluctuations at each grid point. The proposed model is calibrated using experimental uniaxial tensile test results of aluminum alloy (AA) 5754 sheet and then used to predict texture evolution and stress-strain response for balanced biaxial tension and plane-strain tension along rolling (RD) and transverse (TD) directions. The predicted stress-strain and texture results show a good agreement with experimental measurements. The CPU time required by the proposed model is compared with the original EVP-FFT model for two separate cases and the proposed model showed significant improvement in computation time (approximately 100 times faster).

1. Introduction

The response of an aggregate of crystallites of varying size and orientation subjected to plastic deformation is governed by the spatial distribution and dynamics of crystalline defects. The development of advanced characterization tools has enabled very detailed characterization of polycrystalline materials. For example, Scanning Electron Microscopy (SEM) and Transmission Electron Microscopy (TEM) (Lee and Lam, 1996; Nieh et al., 1998; Salem et al., 2003; Armstrong and Walley, 2008; Karel et al., 2016; Wickramarachchi et al., 2016) are used for surface analysis of the material's microstructure. Synchrotron-based X-Ray Diffraction (XRD) and Focus-Ion-Beam (FIB)

combined with Electron Back-Scattering Diffraction (EBSD) are used to measure the chemical composition and crystal structure (Ohashi et al., 2009; Gardner et al., 2010; Abdolvand et al., 2015; Jeong et al., 2015; Erinosho et al., 2016). These advanced experimental techniques bestow highly sophisticated microstructure information and generate large amounts of data creating a difficult task for computational techniques to interpret and harness relevant information. In order to establish the relationship between microstructure and properties of polycrystalline materials undergoing plastic deformation, an accurate prediction of the micromechanical behavior based on directional material properties and gradual development of substructure of the constituent grains is required. Therefore, efficient computational schemes are needed to investigate the microstructure-property relations. In this section, we review crystal plasticity formulations that are extensively used to deal with this challenge.

Among the several crystal plasticity formulations available, the Sachs model (Sachs, 1928) and the Taylor model Taylor (1938) are the earliest epitomes of the so-called mean-field polycrystal models. According to the Taylor model, every crystal is assumed to have the same strain throughout the material, thus the macro strain of the material is simply equal to the local crystal strain. However, while this approach retains the inter-granular compatibility by definition, it leads to violation of inter-granular stress equilibrium. On the contrary, the Sachs model assumes that every crystal experiences the same stress throughout and the local stress is equal to the macro stress. This preserves inter-granular stress equilibrium but it violates inter-granular compatibility. A more realistic approach known as the self-consistent (SC) model, originally proposed by Molinari et al. (1987) for modeling viscoplastic (VP) behavior in polycrystals, accounts for the average interactions of the constituent grains of a polycrystal and has been extensively used to predict texture evolution of polycrystals. This approach was further developed by Lebensohn and Tomé (1993) and Lebensohn et al. (2007). The Viscoplastic Self Consistent (VPSC) model consists in treating each constituent crystal is treated as an Eshelby heterogeneity embedded in a Homogeneous Equivalent Medium (HEM) and has been extensively used for polycrystal modeling accounting for texture-induced plastic anisotropy.

Beyond the formulations discussed above, which rely on mean-field approximations to obtain the plastic response of polycrystalline materials undergoing plastic deformation, full-field approaches are also available, which can predict the actual micromechanical stress and strain fields as well as the effective response of polycrystals with a specific microstructure. Full-field approaches, namely crystal plasticity Finite element method (CP-FEM) and crystal plasticity fast Fourier transform (CP-FFT)-based method, provide richer micromechanical information with direct input from an image of microstructure obtained by EBSD (e.g., Kalidindi et al., 1992, Spowart et al., 2003; Brahme et al.,

2006). Although CP-FEM is a very powerful tool, the size and resolution of the polycrystal that can be treated with this approach are limited, mainly due the large number of degrees of freedom required by CP-FEM computations. An efficient alternative to CP-FEM is given by the CP-FFT. The FFT-based formulation was originally developed by Moulinec and Suquet (1994, 1998) to compute the macro and micro response of composites, that consists of solving the Lippmann-Schwinger equation (Lippmann and Schwinger, 1950) by an iterative method that involves the use of the Green's operator associated to a linear reference medium. The CP-FFT-based schemes have been developed for polycrystalline materials deforming in elastic regime (Brenner et al., 2009), rigid-viscoplastic regime (Lebensohn, 2001; Lebensohn et al., 2008), and elasto-viscoplastic regime (Lebensohn et al., 2012, Grennerat et al., 2012) for infinitesimal strains. Furthermore, the CP-FFT-based methods have been recently extended to finite strains (Eisenlohr et al., 2013; Geus et al., 2016; Kabel et al., 2016).

An explicit or an implicit time-integration scheme can be used to update the rate-dependent constitutive behavior simulated in CP-FEM and FFT-based models. In the various FFT-based techniques available, e.g. Lebensohn et al. (2011), Lebensohn et al. (2012), a modified Newton-Raphson method and augmented Lagrangians procedure based on an implicit integration procedure to iteratively adjust a compatible strain-rate field (or strain field) related to an equilibrated stress has been used. In these FFT-based techniques, the value of temporal step is taken very small. This approach requires relatively longer computational times to reach large deformations. On the other hand, the crystal plasticity models that use semi-explicit time integration schemes are generally more efficient, since larger time steps can be employed in the analysis (e.g. Rashid and Nemat, 1992; Rossiter et al., 2010).

Various researches have shown that CP-FFT methods are more efficient than CP-FEM (e.g. Liu et al., 2010; Prakash and Lebensohn, 2009) in obtaining the response of a polycrystalline material. However, the computationally expensive iterative character of Newton-Raphson type solver and augmented Lagrangians procedure used in most of these FFT-based methods renders them unsuitable for their use in applications that involve larger computational domains deforming under complex strain paths in which large strains are reached (i.e. predictions of forming limit strains). These simulations require highly efficient models to obtain material response expeditiously in order to achieve reasonable computing times. In this paper, a new numerical framework that incorporates the rate-dependent crystal plasticity theory (Asaro and Needleman, 1985) with a semi-explicit forward gradient time-integration scheme (Peirce et al., 1983) into the FFT-based formulation (Lebensohn et al., 2012) is presented. The new model achieves significant gains in terms of computational efficiency over the existing EVP-FFT method (at least 100 times faster).

The plan of this paper is as follows: In section 2, the details of the proposed model are presented. In section 3, the proposed model is benchmarked for the case of an Face Centered Cubic (FCC) polycrystal. Finally, the predictive capability as well as the computational efficiency of the proposed model is demonstrated, where predictions obtained using the proposed model are compared to experiments for the aluminum alloy (AA) 5754.

2. Model formulation

The proposed model obtains the solutions for a heterogeneous volume element chosen to be statistically representative of the whole microstructure. Periodic boundary conditions are enforced across the RVE. For every discrete material point, the numerical analysis employs the tangent method with a semi-explicit integration scheme to find the equilibrated stress and compatible strains through the constitutive relations in a single equilibrium iteration. For completeness, first the rate dependent polycrystal formulation (Asaro and Needleman, 1985) is reviewed, followed by the rate tangent method and the new numerical framework.

2.1 Crystal plasticity model

According to rate dependent polycrystal formulation presented by Asaro and Needleman (1985), for single-phase FCC polycrystals, two distinct physical deformation mechanisms result in total deformation of single crystal. Primarily, the dislocation slip on active slip systems is considered to be the only mechanism responsible for plastic deformation in a single crystal, the elastic distortion and rigid body rotations of crystal lattice with embedded material construct the secondary mode of deformation. Hence, the total deformation gradient can be decomposed into product of plastic deformation gradient embodying dislocation slip and elastic deformation containing lattice distortion as proposed by Lee (1969).

Accordingly, the total deformation gradient $\boldsymbol{F}$ is written as following

$$\boldsymbol{F} = \boldsymbol{F}^{*}\boldsymbol{F}^{\boldsymbol{P}} \tag{1}$$

Where, $\boldsymbol{F}$ is the deformation gradient that satisfies compatibility within each grain and between grains and $\boldsymbol{F}^{\boldsymbol{P}}$ consists of dislocation slip that occurs as plastic shear on twelve slip systems having $\{1\ 1\ 1\}$ slip planes with normal vector $\boldsymbol{m}_{(\alpha)}$ and $\langle 1\ 1\ 0 \rangle$ slip directions with slip vectors $\boldsymbol{s}_{(\alpha)}$ with $1 \leq \alpha \leq 12$ in a FCC crystal. Note that, the brackets for the subscripts α indicate that the quantity is computed over the total number of slip systems. $\boldsymbol{F}^{*}$ embodies elastic deformation and rigid body rotations of crystal lattice.

In the un-deformed state, the lattice vectors $\boldsymbol{m}_{(\alpha)}, \boldsymbol{s}_{(\alpha)}$, are orthonormal and in the deformed state they rotate and stretch as

$$\boldsymbol{m}^*_{(\alpha)} = \boldsymbol{m}_{(\alpha)}\boldsymbol{F}^{*-1}, \qquad \boldsymbol{s}^*_{(\alpha)} = \boldsymbol{F}^*\boldsymbol{s}_{(\alpha)} \tag{2}$$

The velocity gradient is written as sum of its elastic and plastic parts as

$$\boldsymbol{L} = \boldsymbol{L}^* + \boldsymbol{L}^P = \dot{\boldsymbol{F}}\boldsymbol{F}^{-1} \tag{3}$$

where

$$\boldsymbol{L}^* = \dot{\boldsymbol{F}}^*\boldsymbol{F}^{*-1}, \qquad \boldsymbol{L}^P = \boldsymbol{F}^*\left(\dot{\boldsymbol{F}}^P\boldsymbol{F}^{P-1}\right)\boldsymbol{F}^{*-1} \tag{4}$$

Taking the symmetric and antisymmetric parts of the above relations lead to; (i) the elastic strain rate $\boldsymbol{D}^*$ (ii) the plastic strain rate $\boldsymbol{D}^P$, (iii) the so-called plastic spin $\boldsymbol{W}^P$, and (iv) the spin $\boldsymbol{W}^*$ associated with the rigid lattice rotation. Accordingly, the total strain rate and spin tensors can be written as,

$$\boldsymbol{D} = \boldsymbol{D}^* + \boldsymbol{D}^P \tag{5}$$

$$\boldsymbol{\Omega} = \boldsymbol{\Omega}^* + \boldsymbol{\Omega}^P \tag{6}$$

By introducing the following symmetric $\boldsymbol{P}_{(\alpha)}$ and skew symmetric $\boldsymbol{W}_{(\alpha)}$ second order tensors for each slip system α,

$$\boldsymbol{P}_{(\alpha)} = \frac{1}{2}\left[\boldsymbol{s}^*_{(\alpha)} \otimes \boldsymbol{m}^*_{(\alpha)} + \boldsymbol{m}^*_{(\alpha)} \otimes \boldsymbol{s}^*_{(\alpha)}\right] \tag{7}$$

$$\boldsymbol{W}_{(\alpha)} = \frac{1}{2}\left[\boldsymbol{s}^*_{(\alpha)} \otimes \boldsymbol{m}^*_{(\alpha)} - \boldsymbol{m}^*_{(\alpha)} \otimes \boldsymbol{s}^*_{(\alpha)}\right] \tag{8}$$

the plastic strain rate $\boldsymbol{D}^P$ and plastic spin $\boldsymbol{\Omega}^P$ for the crystal can be written as

$$\boldsymbol{D}^P = \sum_{\alpha} \boldsymbol{P}_{(\alpha)}\,\dot{\gamma}_{(\alpha)}, \qquad \boldsymbol{\Omega}^P = \sum_{\alpha} \boldsymbol{W}_{(\alpha)}\,\dot{\gamma}_{(\alpha)} \tag{9}$$

where $\dot{\gamma}_{(\alpha)}$ is the shear rate on each slip system α. The constitutive equation for a crystal is specified by the Jaumann rate of the Kirchoff stress, $\boldsymbol{\tau}$, as

$$\overset{\nabla}{\boldsymbol{\tau}} = \boldsymbol{\mathcal{L}}\colon\boldsymbol{D} - \sum_{\alpha} \boldsymbol{R}_{(\alpha)}\,\dot{\gamma}_{(\alpha)} \tag{10}$$

where, $\boldsymbol{\mathcal{L}}$ is the fourth order tensor of elastic moduli based on the anisotropic elastic constants of the FCC crystals which exhibits the appropriate cubic symmetry and, $\boldsymbol{R}_{(\alpha)}$ is the second-order tensor given as

$$\boldsymbol{R}_{(\alpha)} = \boldsymbol{\mathcal{L}}\colon\boldsymbol{P}_{(\alpha)} + \mathbf{W}_{(\alpha)}\boldsymbol{\tau} - \boldsymbol{\tau}\boldsymbol{W}_{(\alpha)} \tag{11}$$

In order to complete the constitutive description, the shear rate on each slip system needs to be defined. The shear rate $\dot{\gamma}_{(\alpha)}$ on each slip system α is governed by a power-law expression, so that

$$\dot{\gamma}_{(\alpha)} = \dot{\gamma}_0 \, sgn \, \tau_{(\alpha)} \left| \frac{\tau_{(\alpha)}}{g_{(\alpha)}} \right|^{1/m} \tag{12}$$

where $\tau_{(\alpha)}$ is the resolved shear stress, $g_{(\alpha)}$ is the hardness, of slip system α, $\dot{\gamma}_0$ is the reference shear rate (same for each slip system) and m is the index of strain rate sensitivity. The hardened state of each slip system $\boldsymbol{\alpha}$ is characterized by $g_{(\alpha)}$. The hardening rate, $\dot{g}_{(\alpha)}$, for multiple slip is defined by hardening law as following

$$\dot{g}_{(\alpha)} = \sum_{\beta} \boldsymbol{h}_{\alpha\beta} |\dot{\gamma}_{\beta}| \tag{13}$$

where, $\boldsymbol{h}_{(\alpha\beta)}$ is the hardening moduli and $\dot{\gamma}_{(\beta)}$ is the single slip shear stress rate on slip system β. The hardening moduli used here is the one that has been used previously by Peirce et al. (1983) and Asaro and Needleman (1984),

$$\boldsymbol{h}_{(\alpha\beta)} = \boldsymbol{q}_{(\alpha\beta)} h_{(\beta)} \text{ (no sum on } \beta) \tag{14}$$

where $q_{\alpha\beta}$ matrix describes the latent hardening of the crystallite and h_{β} is the single slip hardening. Following (Asaro and Needleman, 1985), it is considered that g_{α} depends on the accumulated sum, γ_a, of the slips, where

$$\gamma_{(a)} = \int_0^t \sum_{\alpha} |\dot{\gamma}_{(\alpha)}| dt \tag{15}$$

The model presented by Chang and Asaro (1981) is employed to calculate the single slip hardening. Accordingly,

$$h_{(\beta)} = h_s + (h_0 - h_s) sech^2 \left\{ \left(\frac{h_0 - h_s}{\tau_s - \tau_0} \right) \gamma_{(a)} \right\} \tag{16}$$

where τ_0 is the critical resolved shear stress, τ_s is the value of saturated shear stress, h_s is the asymptotic hardening rate of slip systems and h_0 is the hardening constant.

2.2 Rate tangent modulus method

The new numerical framework developed in this research employs the semi-explicit rate tangent modulus method developed by Peirce et al. (1983). According to this method, the increment in slip on each slip system α at time t is given by

$$\Delta\gamma_{(\alpha)} = \gamma_{(\alpha)}^{t+\Delta t} - \gamma_{(\alpha)}^{t} \tag{17}$$

Within the time increment Δt, a linear interpolation of slip increment is employed to give

$$\Delta\gamma_{(\alpha)} = \left[(1-\theta)\,\dot{\gamma}^{t}_{(\alpha)} + \theta\,\dot{\gamma}^{t+\Delta t}_{(\alpha)}\right]\Delta t \tag{18}$$

where θ is an interpolation parameter ranging between 0 and 1. $\theta = 0$ corresponds to Euler time stepping scheme ($\theta = 0.5$ is used in the current formulation). The last term in above equation can be approximated by using Taylor series expansion as

$$\dot{\gamma}^{t+\Delta t}_{(\alpha)} \cong \dot{\gamma}^{t}_{(\alpha)} + \left.\frac{\partial\dot{\gamma}_{(\alpha)}}{\partial\tau_{(\alpha)}}\right|_{t}\Delta\tau_{(\alpha)} + \left.\frac{\partial\dot{\gamma}_{(\alpha)}}{\partial g_{(\alpha)}}\right|_{t}\Delta g_{(\alpha)} \tag{19}$$

Equation 19 can be further simplified as (Peirce et al., 1983);

$$\sum_{\beta}\boldsymbol{N}_{(\alpha\beta)}\Delta\gamma_{(\beta)} = \left(\dot{\gamma}^{t}_{(\alpha)} + \boldsymbol{Q}_{(\alpha)}:\boldsymbol{D}\right)\Delta t \tag{20}$$

where $\dot{\gamma}^{t}_{(\alpha)}$ can be calculated by equation (12) and $\boldsymbol{Q}_{\alpha}$ is given as

$$\boldsymbol{Q}_{(\alpha)} = \left(\frac{\theta\Delta t\,\dot{\gamma}^{t}_{(\alpha)}}{m\tau_{(\alpha)}}\right)\boldsymbol{R}_{(\alpha)} \tag{21}$$

and

$$\boldsymbol{N}_{(\alpha\beta)} = \boldsymbol{\delta}_{(\alpha\beta)} + \left(\frac{\theta\Delta t\,\dot{\gamma}^{t}_{(\alpha)}}{m}\right)\times\left[\frac{\boldsymbol{R}_{(\alpha)}:\boldsymbol{P}_{(\beta)}}{\tau_{(\alpha)}} + sgn(\tau_{(\beta)})\frac{\boldsymbol{h}_{(\alpha\beta)}}{g_{(\alpha)}}\right] \tag{22}$$

Denoting the inverse of $N_{(\alpha\beta)}$ by $M_{(\alpha\beta)}$ and then inverting equation (22) leads to a simpler form

$$\Delta\gamma_{(\alpha)} = \left[\dot{f}_{(\alpha)} + \boldsymbol{\chi}_{(\alpha)}:\boldsymbol{D}\right]\Delta t \tag{23}$$

where

$$\dot{f}_{(\alpha)} = \sum_{\beta}\boldsymbol{M}_{(\alpha\beta)}\,\dot{\gamma}^{t}_{(\alpha)} \;\; and \;\; \boldsymbol{\chi}_{(\alpha)} = \sum_{\beta}\boldsymbol{M}_{(\alpha\beta)}\boldsymbol{Q}_{(\alpha)} \tag{24}$$

The equation (23) allows equation (10) to be written as

$$\overset{\nabla}{\boldsymbol{\tau}} = \boldsymbol{\mathcal{C}}:\boldsymbol{D} - \sum_{\alpha}\boldsymbol{R}_{(\alpha)}\dot{f}_{(\alpha)} \tag{25}$$

where $\boldsymbol{\mathcal{C}}$ is the elasto-viscoplastic moduli given as

$$\boldsymbol{\mathcal{C}} = \boldsymbol{\mathcal{L}} - \sum_{\alpha}R_{(\alpha)}\,\boldsymbol{\chi}_{(\alpha)} \tag{26}$$

Note that, for $\theta = 0$ the equation (25) reduces to equation (10). Now, expressing constitutive equation (25) in form of Jaumann rate $\overset{\nabla}{\boldsymbol{\sigma}}$ of Cauchy stress $\boldsymbol{\sigma}$

$$\overset{\nabla}{\boldsymbol{\sigma}} = \boldsymbol{\mathcal{C}}\colon \boldsymbol{D} - \dot{\boldsymbol{\sigma}}^{0} - \boldsymbol{\sigma}\, tr\boldsymbol{D} \tag{27}$$

Since, $\boldsymbol{\sigma} = \det \boldsymbol{F}^{-1}\, \boldsymbol{\tau}$, the viscoplastic stress-rate is given by

$$\dot{\boldsymbol{\sigma}}^{0} = \sum_{\alpha} \boldsymbol{R}_{(\alpha)}\, \dot{\gamma}_{(\alpha)} \tag{28}$$

Now, updating the Cauchy stress tensor for next time step as following

$$\boldsymbol{\sigma}^{t+\Delta t} = \boldsymbol{\sigma}^{t} + \dot{\boldsymbol{\sigma}}^{0}\, \Delta t \tag{29}$$

The sections above describe the general Asaro and Needleman (1985) framework that has been used in various homogenization as well as in full-field schemes (Inal, 2002; Inal et al., 2010; Brahme et al., 2011; Izadbakhsh et al., 2011; Inal and Mishra, 2012; Cyr et al., 2015; Muhammad et al., 2015; Pinna et al., 2015). This formulation, coupled with a rate tangent semi-explicit integration scheme is implemented into a FFT-based model as described next.

2.3 FFT model and implementation of the new crystal plasticity framework

To predict the evolution of micromechanical fields and intragranular texture during deformation, the space resolved configuration of the regular Fourier grid points and the grain interactions must be taken into account in the whole RVE. In proposed numerical approach, each Fourier grid point represents a voxel inside a grain. The Fourier grid $\{x_{\mathrm{d}}\}$ is defined as

$$\{x_d\} = \left\{ \left((I_1 - 1)\frac{\ell_1}{N_1}, (I_2 - 1)\frac{\ell_2}{N_2}, (I_3 - 1)\frac{\ell_3}{N_3} \right);\ I_k = 1, \dots, N_k, k = 1,3 \right\} \tag{30}$$

where ℓ_{k} is the length of the grid and $\mathrm{N_k}$ is the number of Fourier points in each direction k. Note that, from this point onward, index notation will be employed in the formulations. In order to account for the interaction of each grid point with all the other points in the RVE, the following problem for heterogeneous RVE needs to be solved at each grid point written as following:

$$\begin{cases} \sigma_{ij}(x) = \mathcal{L}_{ijkl}(x)\varepsilon_{kl}(x), \qquad \forall x \in \{x_d\} \\ \sigma_{ij,j}(x) = 0 \\ Periodic\ boundary\ conditions\ across\ RVE \end{cases} \tag{31}$$

where $\varepsilon_{kl}(x)$ and $\sigma_{ij}(x)$ are the local strain and local stress fields and $\mathcal{L}_{ijkl}(x)$ is the local elastic stiffness. The total local strain is given by

$$\varepsilon_{ij}(x) = \tilde{\varepsilon}_{ij}(x) + E_{ij} \tag{32}$$

where $\tilde{\varepsilon}_{ij}(x)$ is the strain fluctuation in the crystal due to heterogeneity and E_{ij} is the strain imposed on the RVE. The local strain fluctuation can be found using Green function method if local stress

fluctuation field is known. Finding local stress fluctuation involves $\mathcal{L}^0$, an average elastic moduli of a linear reference medium. Here, linear medium refers to medium that is not yet loaded or is in the un-deformed state.

Accordingly, the stress tensor can be written as;

$$\sigma_{ij}(x) = \sigma_{ij}(x) + \mathcal{L}^0_{ijkl}\varepsilon_{kl}(x) - \mathcal{L}^0_{ijkl}\varepsilon_{kl}(x) \tag{33}$$

or,

$$\sigma_{ij}(x) = \mathcal{L}^0_{ijkl}\varepsilon_{kl}(x) + \tilde{\sigma}_{ij}(x) \tag{34}$$

where, $\tilde{\sigma}_{ij}(x)$ is the stress fluctuation and is given by:

$$\tilde{\sigma}_{ij}(x) = \sigma_{ij}(x) - \mathcal{L}^0_{ijkl}\varepsilon_{kl}(x) \tag{35}$$

The strain tensor ε_{kj} is related to displacement gradient $u_{k,l}(x)$ as

$$\varepsilon_{kl} = \left(u_{k,l}(x) + u_{k,l}(x)\right)/2 \tag{36}$$

Thus, the local problem for heterogeneous RVE becomes:

$$\begin{cases} \sigma_{ij}(x) = \mathcal{L}^0_{ijkl}\varepsilon_{kl}(x) + \tilde{\sigma}_{ij}(x), & \forall x \in \{\chi_d\} \\ \sigma_{ij,j}(x) = 0 \\ Periodic\ boundary\ conditions\ across\ RVE \end{cases} \tag{37}$$

To satisfy equilibrium locally, the divergence of local Cauchy stress tensor must be equal to zero, i.e.,

$$\mathcal{L}^0_{ijkl}\varepsilon_{kl,j}(x) + \tilde{\sigma}_{ij}(x) = 0 \tag{38}$$

The Green's function method is used to solve the equilibrium equation (38) for an applied strain E_{ij} that requires the solution of following problem (Lebensohn et al., 2012):

$$\mathcal{L}^0_{ijkl}\mathrm{G}_{km,lj}(x - x') + \delta_{im}\delta(x - x') = 0 \tag{39}$$

where $\mathrm{G}_{km,lj}(x - x')$ is the Green's function associated with the displacement field. Accordingly, the local strain fluctuations can be expressed as convolutions in the real space so that

$$\tilde{\varepsilon}_{kl}(x) = \int_{R^3} \mathrm{G}_{ki,jl}(x - x')\tilde{\sigma}_{ij}(x')dx' \tag{40}$$

Since a convolution integral in real space can be expressed as a product in the Fourier space for a regular Fourier grid, equation (40) is solved in the Fourier space that renders the FFT-based implementations computationally efficient for computing the local response. Using the convolution theorem, the local strain fluctuations in Fourier space are given by

$$\hat{\tilde{\varepsilon}}_{kl}(\xi) = \hat{\Gamma}^0_{ijkl}(\xi))\hat{\tilde{\sigma}}_{kl}(\xi) \tag{41}$$

where "^" indicates Fourier transform, and ξ is the frequency point in the Fourier space. Furthermore, the Green operator in Fourier space $\hat{\Gamma}^0_{ijkl}$, which is a function of the stiffness tensor of the reference medium and the frequency, is given by

$$\hat{\Gamma}^0_{ijkl}(\xi) = -\xi_j\xi_l\hat{G}_{ik}(\xi), \qquad \hat{G}_{ik}(\xi) = \left[\mathcal{L}^0_{ijkl}\xi_l\xi_j\right]^{-1} \tag{42}$$

Accordingly, the local strain fluctuations in real space can be obtained by taking the inverse Fourier transform of equation (41) such as

$$\tilde{\varepsilon}_{kl}(x) = fft^{-1}(sym(\hat{\Gamma}^0_{ijkl}(\xi))\hat{\tilde{\sigma}}_{kl}(\xi))$$

As a part of augmented Lagrangians iterative procedure, Michel et al. (2001) proposed an alternative method in which the Fourier transform of local stress tensor is computed instead of local perturbation field. This approach is employed in the single iteration procedure presented in this paper. Accordingly, the total local strain is given by

$$\varepsilon_{ij}(\mathrm{x}) = fft^{-1}(sym(\hat{\Gamma}^0_{ijkl}(\xi))\ \hat{\sigma}_{kl}(\xi)) + E_{ij} \tag{43}$$

In the new numerical framework, to calculate the local stress at each material point, the rate tangent method is used to update the rate form of the constitutive equation in a single iteration for equilibrium, (i.e., equation (25)). At first time step, with an imposed macro strain E_{ij}, the algorithm can be initialized with zero strain fluctuation, $\tilde{\varepsilon}_{ij}(x) = 0$ and $\sigma^t_{ij}(x) = \mathcal{C}^t_{ijkl}(x)D^t_{kl}(x)$. For next temporal increment, the algorithm computes the:

1. Current guess of local Cauchy stress $\sigma^{t+\Delta t}_{ij}(x)$ using rate tangent scheme,
2. Fourier transform of current guess of Cauchy stress, $\hat{\sigma}^{t+\Delta t}_{ij}(\xi) = fft\left(\sigma^{t+\Delta t}_{ij}(x)\right)$,
3. Green operator ($\hat{\Gamma}^0_{ijkl}(\xi)$) as a function of reference medium stiffness ($\mathcal{L}^0_{ijkl}$) for each frequency (ξ) as given by equation (42),
4. Local strain fluctuation, $\tilde{\varepsilon}^{t+\Delta t}_{ij}(x) = fft^{-1}(sym(\hat{\Gamma}^0_{ijkl}(\xi))\ \hat{\sigma}_{kl}(\xi))$,
5. Total local strain as, given by equation (38),
6. Updates of the current local strain rate tensor $D^{t+\Delta t}_{ij}(x)$ and the current Cauchy stress tensor $\sigma^{t+\Delta t}_{ij}(x)$ using rate tangent scheme,

The algorithm then repeats steps 1-6 for the next temporal increments.

3. Model calibration and validation

In this section, the proposed numerical model is validated by comparing the predictions from the new model with the predictions obtained from the well-established elasto-viscoplastic fast Fourier transform (EVP-FFT) model (Lebensohn et al., 2012) . The numerical analyses are carried out for a copper polycrystal and an artificial random FCC polycrystal with anisotropic constants, A=2.2 and A=0.5 respectively ($A = (2 \times C_{44}) / (C_{11}-C_{12})$). The corresponding elastic constants employed in these analyses are presented in Table 1. For both cases, the same representative volume element (RVE) is used where 100 grains with randomly assigned copper orientations are employed in a regular grid of 16 x 16 x 16 Fourier points (to discretize the RVE, Fig. 1).

Table 1. Adopted elastic constants for copper polycrystal (Simmons and Wang, 1971) and for an artificial polycrystal (Lebensohn et al., 2012).

Elastic constants	C_{11}	C_{12}	C_{14}
Copper polycrystal	170.2 GPa	114.9 GPa	61.0 GPa
Artificial polycrystal	233.6 GPa	88.2 GPa	33.8 GPa

It should be mentioned that the same material parameters and boundary conditions are used for both models during each set of simulations. The polycrystals deform plastically by slip on twelve slip systems for a critical resolved shear stress (CRSS), τ_0, of 10 MPa (no strain-hardening is assumed) and the strain rate sensitivity index, *m*, is set to 0.1. The simulations are carried out up to a strain of 0.2% with an applied strain rate of 10^{-4} s^{-1} along the rolling direction (RD). Note that, from now on, the new model will be referred to as RTCP-FFT model.

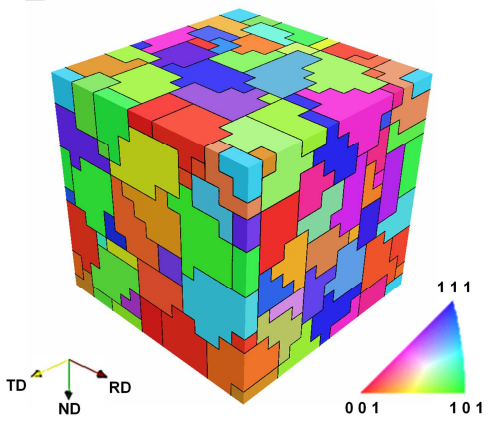

Fig. 1. The synthesized microstructure of copper polycrystal and for an artificial FCC polycrystal with 16 x 16 x 16 Fourier points in 100 grains showing initial texture distribution.

Fig. 2 shows the equivalent stress–strain curves predicted by the EVP-FFT model, while Figs. 3 (a-b) present comparisons between the predictions obtained from the EVP-FFT and the RTCP-FFT models. Note that, for these simulations, the main interest is the elasto-viscoplastic transition zone, which varies with anisotropic constants. For both the analyses (for a copper polycrystal and the artificial FCC polycrystal) the simulations with the RTCP-FFT model are in excellent agreement with the predictions obtained from the EVP-FFT.

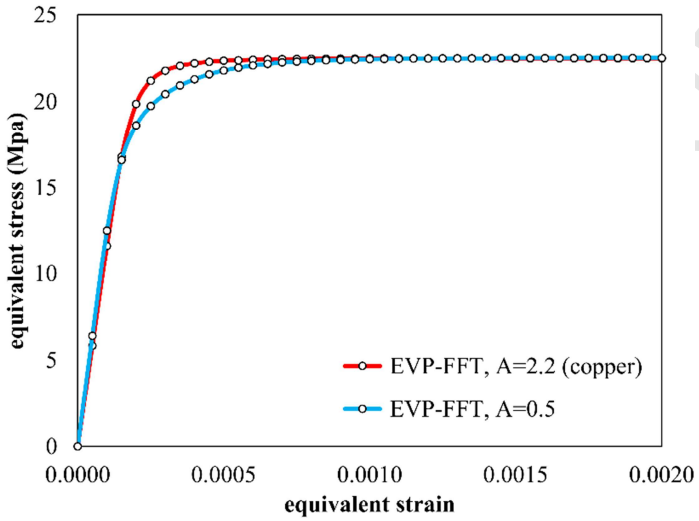

Fig. 2. Predicted von Mises equivalent stress–strain curves during uniaxial tension along RD using the EVP-FFT model for cases of the copper polycrystal and an artificial FCC polycrystal.

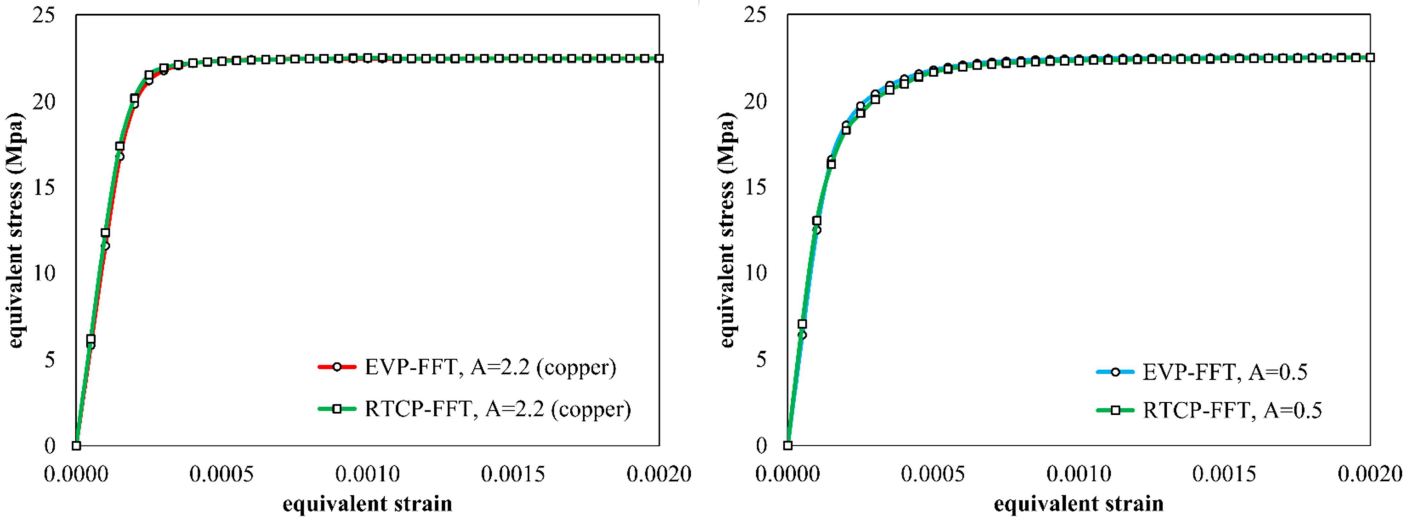

(a) (b)

Fig. 3. Comparisons of the predicted von Mises equivalent stress–strain curves during uniaxial tension along RD between the RTCP-FFT and EVP-FFT models for; (a) copper polycrystal, and (b) an artificial polycrystal.

Next, for the case of the copper polycrystal, the predicted local micromechanical fields obtained with both models obtained at an equivalent strain of 5% are compared (Figs. 4a-d). A qualitative comparison of the results shows that the proposed model reproduces similar micromechanical fields as compared to the original EVP-FFT model (Fig. 4); the locations of deviations from uniform stress and strain fields predicted by the RTCP-FFT model, in general, are also in reasonable agreement with those predicted by the original EVP-FFT model. However, significant variations are observed between the computed local strains at some locations. These variations are mainly due to the different numerical integration schemes employed in the models. Furthermore, to quantify the variations, the mismatch in terms of both the local equivalent strains and the local equivalent stresses, normalized by the sum of local equivalent fields i.e. strains or stresses on all the voxels, are presented in the Fig. 5. The normalized difference is calculated per voxel as

$$Mismatch\ in\ local\ fields\ at\ voxel\ i = \frac{2 * \left| Field_i^{EVP-FFT} - Field_i^{RTCP-FFT} \right|}{\sum_{i=1}^{N} Field_i^{EVP-FFT} + \sum_{i=1}^{N} Field_i^{RTCP-FFT}}$$

where N is the total number of voxels. It should be mentioned that even though the local fields calculated by the RTCP-FFT model can be different from those computed by the EVP-FFT model, these differences have a very little impact, if any, on the macroscopic behavior (Fig. 3a).

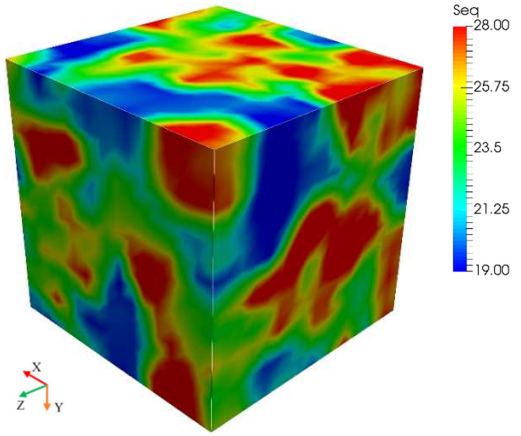

(a) EVP-FFT (vM stress)

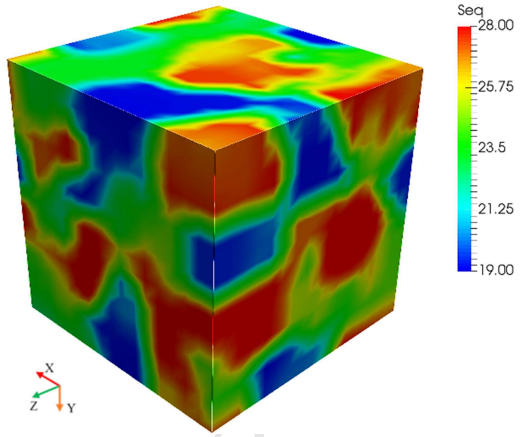

(b) RTCP-FFT (vM stress)

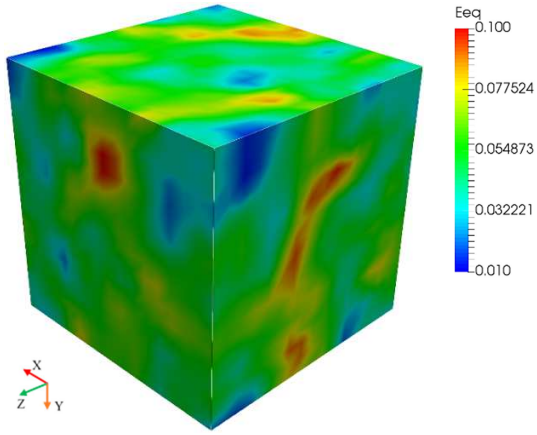

(c) EVP-FFT (equivalent strain)

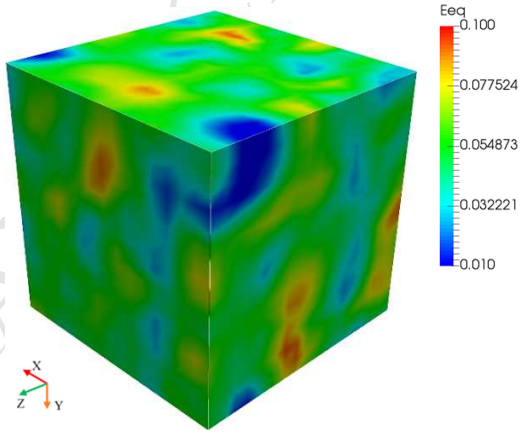

(d) RTCP-FFT (equivalent strain)

Fig. 4. Comparison of the simulated micromechanical fields for the copper polycrystal (A = 2.2) at 5% equivalent strain during uniaxial tension along RD ; *(a-b)* – distribution of the von Mises equivalent stress (MPa), (*c-d)* – distribution of equivalent strain.

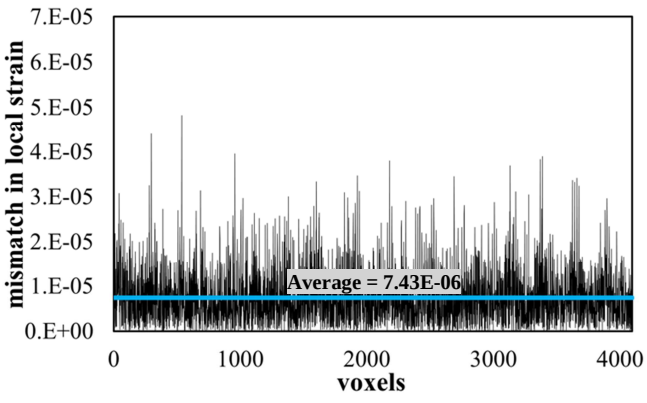

(a)

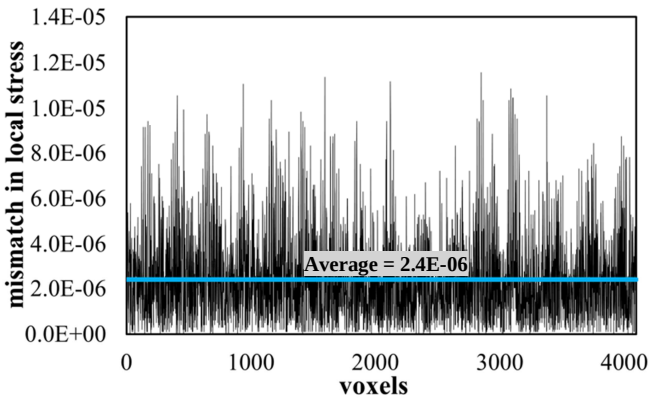

(b)

Fig. 5. Comparison of variations in the local fields for each voxel between the RTCP-FFT and the EVP-FFT models in copper polycrystal (A = 2.2) at 5% equivalent strain during uniaxial tension along RD: (a) mismatch in the local equivalent strain, (b) mismatch in the local equivalent stress.

4. Application to Aluminum Alloy (AA) 5754

In this section, the predictive capability of the new model is demonstrated by comparing predictions from the new model with experiments for the commercial aluminum alloy (AA) 5754. It is important to mention that the proposed model is only calibrated for uniaxial tension along RD, then the same parameters are employed for the predicting the macroscopic stress-strain responses and the texture evolution for various other strain paths. For each case, the predictions obtained with RTCP-FFT model are compared with the measured data presented in Hu et al. (2012).

4.1 Model setup

In this analysis, a representative volume element (RVE) with 128 x 128 x 128 points that represent 8837 equiaxed grains is used to model AA5754 (Fig. 6e). The pole figures and orientation distribution functions (ODF) of the initial texture of as received O-temper AA5754 are presented in Figs. 6 (a-d). The synthetic microstructure in the RVE with equiaxed grains is built using a microstructure building software as proposed by Brahme et al. (2006). In this approach, an optimization technique is used to minimize the error, in both orientation distribution function (ODF) and misorientation distribution function (MDF), between measured and assigned orientations.

4.2 Boundary conditions

Simulations of uniaxial tension, balanced biaxial tension and plane strain tension are performed in this section. Uniaxial tension is simulated by applying a velocity gradient in RD (X) and TD (Y) directions respectively while the remaining components of the velocity gradient are kept unconstrained. Equibiaxial tension is simulated by applying a velocity gradient in both RD-TD (X-Y) directions while keeping ND (Z) direction unconstrained. Similarly, plane strain tension is simulated by applying a velocity gradient in the RD (X) and TD (Y) directions respectively while constraining the ND (Z) direction.

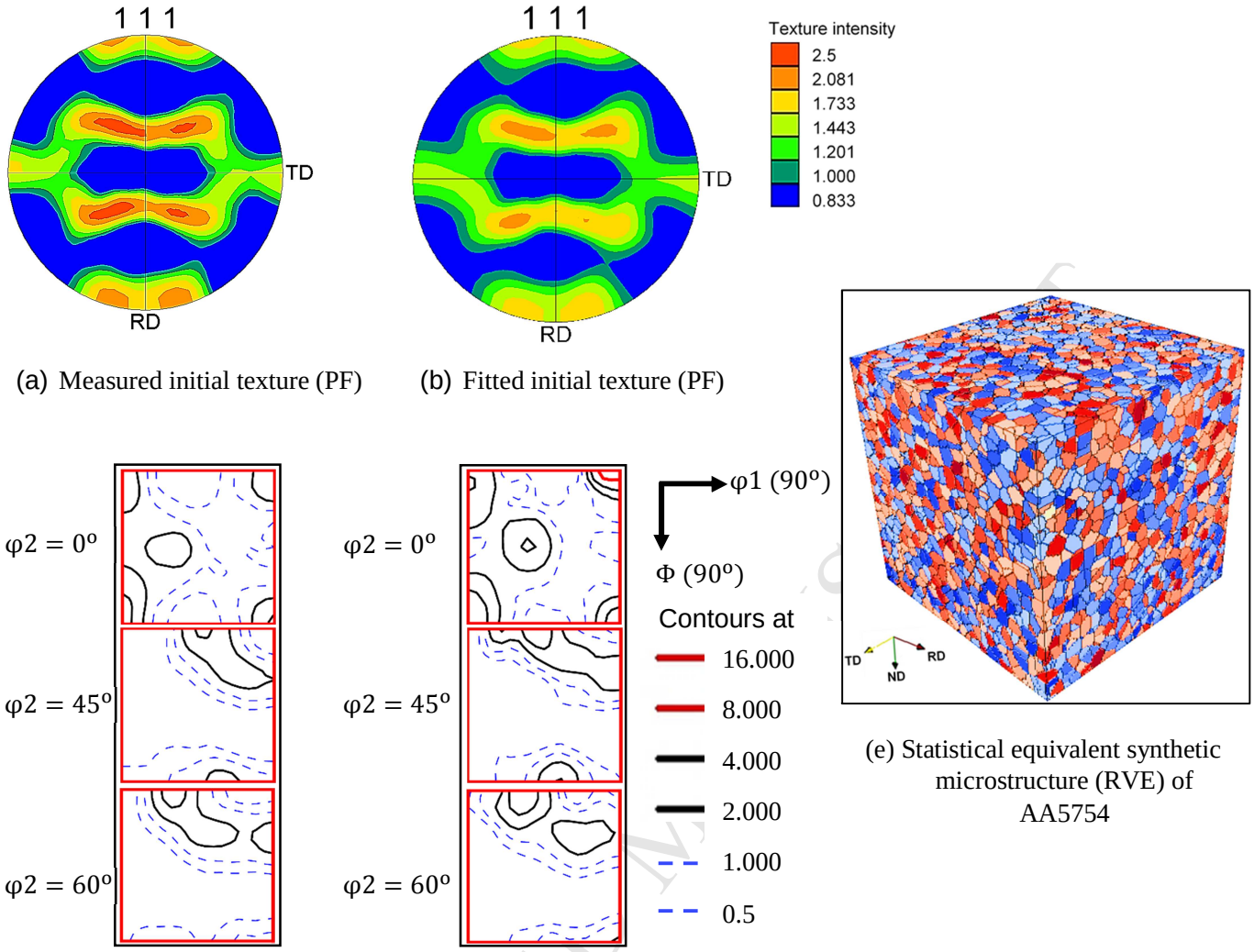

Fig. 6. Comparison of initial texture: (a) pole figure representations of the as-received experimental texture and (b) fitted texture; Comparison of contours of experimental ODFs (c) and fitted ODFs (d) at 0, 45, and 60 degrees of $\varphi 2$ sections. (e) The generated microstructure with 128 x 128 x 128 points in 8837 equiaxed grains, the colors represent different grains.

4.3 Model calibration

An initial curve fitting of the macroscopic stress-strain response of the polycrystalline is performed for uniaxial tensile test to calibrate the RTCP-FFT model (Fig. 6a), and the material parameters employed in the model are presented in Table 2. Note that, the same set of material parameters (as presented in Table 2) are employed in all of the simulations presented in section 4.

Table 2. Constitutive parameters used to calibrate RTCP-FFT model for uniaxial tension along RD.

h_0/τ_0	τ_s/τ_0	τ_0	h_s/τ_0	m	q
10.0	2.24	25.5	1.9	0.02	1.0

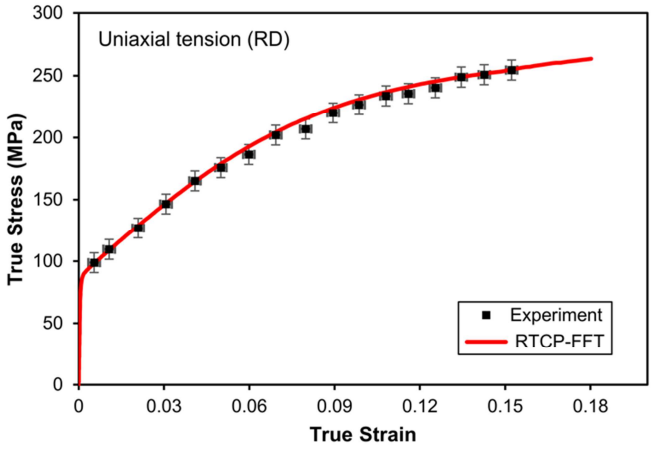

(a) Comparison of simulated and measured stress-strain curves for uniaxial tension after 15 % true strain along RD

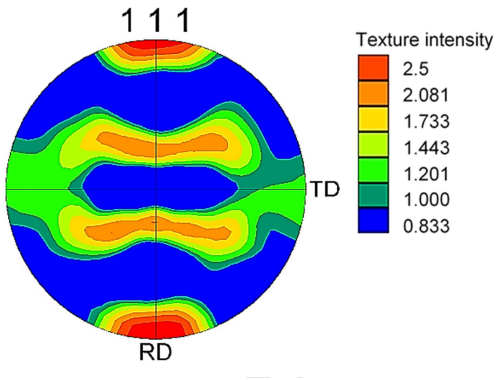

(b) Pole figure of simulated texture for uniaxial tension after 15 % true strain along RD

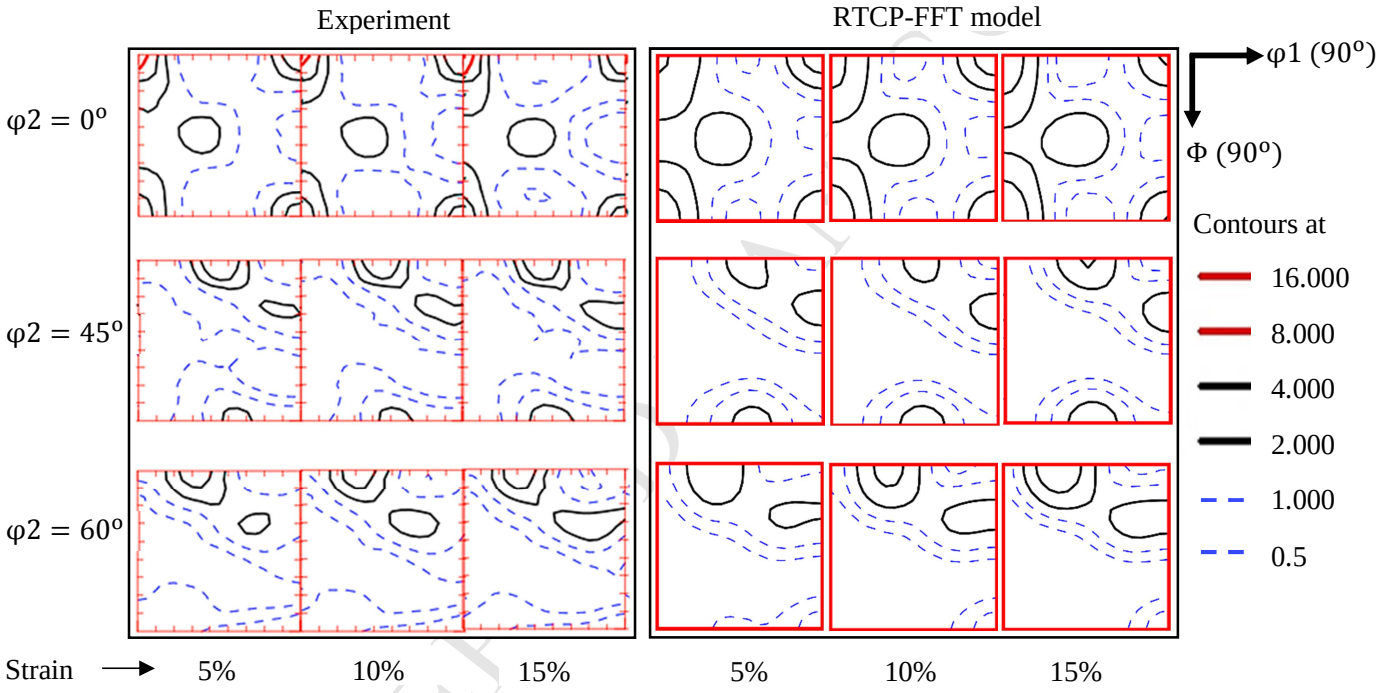

(c) ODF sections of measured texture for uniaxial tension along RD (Hu et al., 2011)

(d) ODF sections of simulated texture for uniaxial tension along RD

Fig. 7. (a) Comparison of macroscopic stress strain curves of measured data (Hu et al., 2011) and simulated response by calibrated-RTCP-FFT model for RD-uniaxial tension. (b) Simulated texture in form of pole figure for RD-uniaxial tension after 15% true strain. (c) and (d) Comparison of ODF sections of measured and simulated texture for RD-uniaxial tension at 5%, 10 % and 15% true strain.

The predicted texture evolution for 15 % strain during uniaxial tension along RD is presented in Fig. 7b, while Figs. 7 (c-d), present a comparison of ODF sections of measured and predicted evolved texture at different levels of true strain. Results show that the RTCP-FFT model can accurately capture the major trends of texture evolution. Both the experimentally measured and the predicted texture

(evolved) show an increase in the intensity of Copper and S (typical rolling textures) as the deformation proceeds from 5% to 15% uniaxial tension.

4.4 Simulations of balanced biaxial tension and plane strain tension

In this section, the RTCP-FFT model is employed to simulate the stress-strain response of AA5754 during; balanced biaxial tension, plane strain tension along RD, uniaxial tension and plane strain tension along TD. The predictions are compared with those determined experimentally. The numerical analyses show that the RTCP-FFT model can accurately predict the macroscopic stress-strain response of AA5754 for the above mentioned strain paths (Figs. 8a-d). Recently, Hu et al. (2012), presented a similar study for AA5754 where they used a Taylor based model, VPSC model and VP-FFT model. While their predictions were also in good agreement with experiments, it should be mentioned that they employed a single set of hardening parameters that was obtained by simultaneously curve fitting the simulations to all the different experimental strain paths (uniaxial tension, balanced biaxial tension, plane strain tension). Contrary to their approach, all the predictions presented in this section employ the same set of parameters (Table 2) obtained from a single curve fit for uniaxial tension. Thus, the RTCP-FFT model can accurately predict the macroscopic stress-strain response for various strain paths with a single set of parameters that are directly obtained from an experimental uniaxial stress-strain curve.

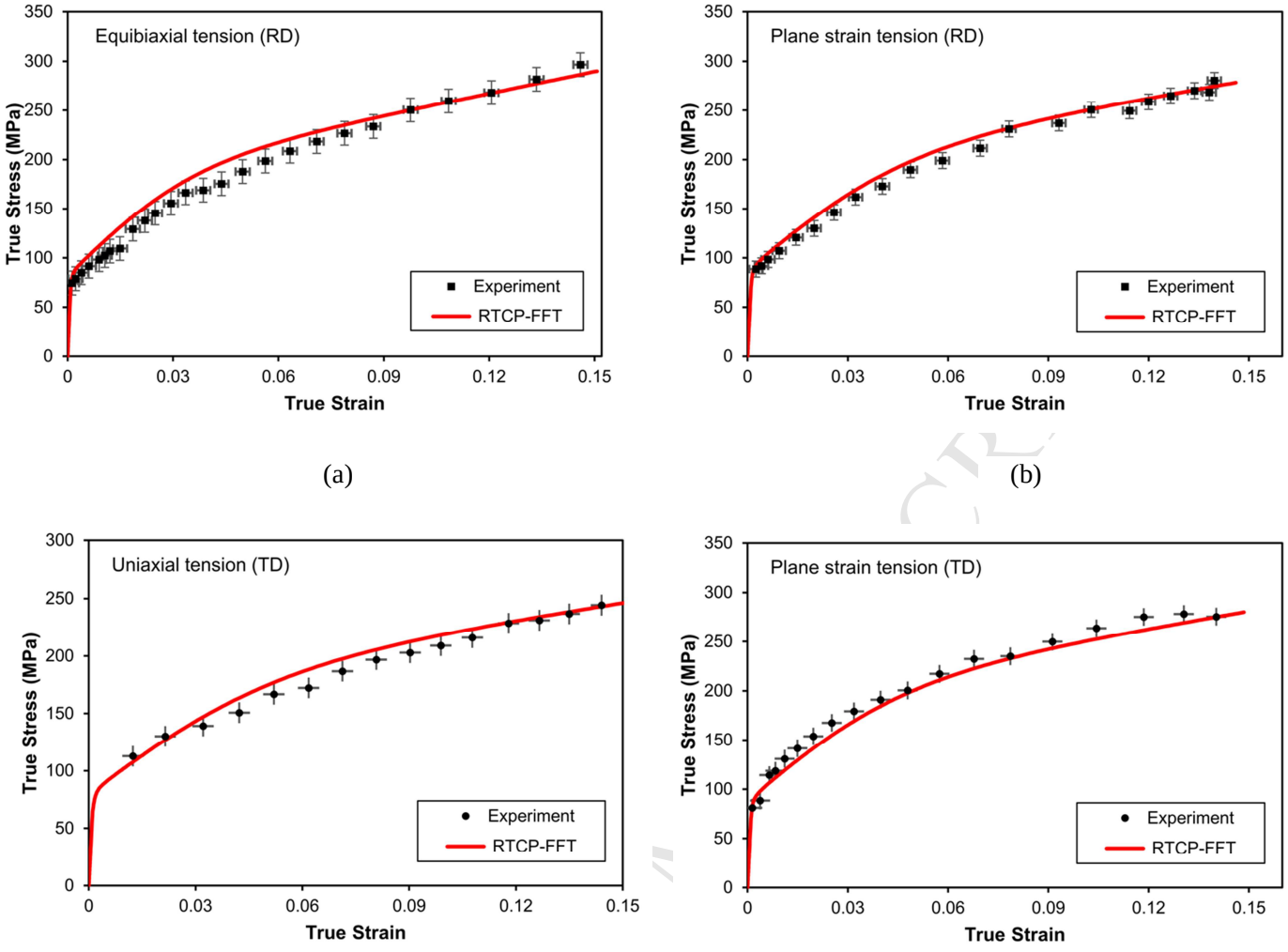

Fig. 8. Comparison of predicted and measured (Hu et al., 2011) stress-strain curves for four different strain paths after 15 % true strain; (a) equibiaxial tension (σ_{11} , e_{11}), (b) plane-strain tension in RD (σ_{11}, e_{11}), (c) Uniaxial tension in TD (σ_{22} , e_{22}) and (d) plane strain tension in TD (σ_{22} , e_{22}).

4.5 Predictions of texture evolution

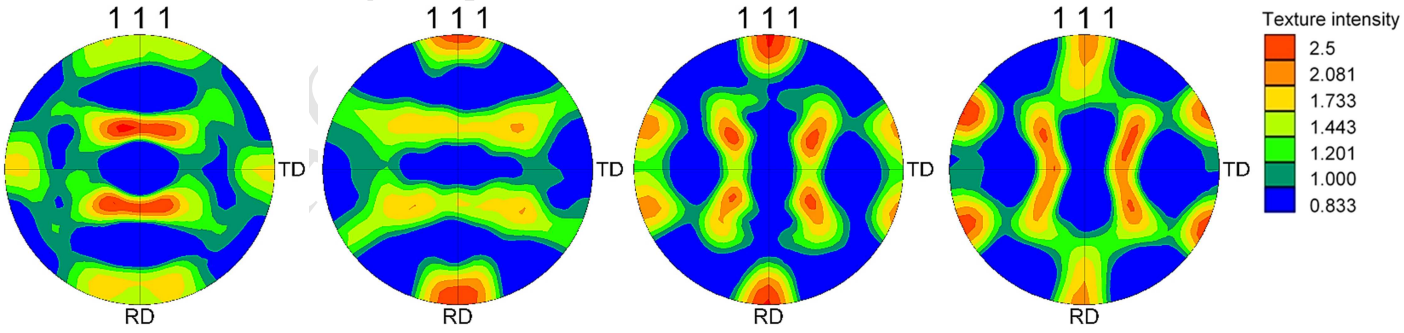

Fig. 9. Comparison of predicted texture in form of pole figures for four different strain paths; (a) equibiaxial tension, (b) plane strain tension along RD, (c) uniaxial tension along TD and (d) plane strain tension along TD.

The RTCP-FFT model is also employed to predict texture evolution (Fig. 9). The initial texture (Fig. 6b) contains higher amounts of Brass, Cube and S compared to Copper and Goss texture components. In the predicted texture after 15% true strain, an increase in Brass is observed in balanced biaxial tension and uniaxial tension along TD with a decrease in the intensities of cube and S. On the other hand, Copper component is strengthened after 15% strain in cases of plane strain tension along RD and TD. Overall, a smaller change is observed in intensities of texture components from their initial values in uniaxial tension and plane strain tension cases.

Next, an analysis of texture evolution is presented using ODF sections. The predicted texture evolutions are compared with experimental measurements (Hu et al., 2011) at 5%, 10% and 15% true strain. Figs. 10-13 show the progress of ODF with strain during balanced biaxial tension, plane strain tension along RD and TD respectively as well as in uniaxial tension along TD. Simulations show that, as the deformation progresses, the grains favor the formation of Brass and Cube orientations during uniaxial tension along TD, the grains tend to form the Brass in case of plane strain tension along TD and the β-fiber rolling texture is further strengthened in plane strain tensions along RD. In case of balanced biaxial tension, a stronger growth of Brass and Copper components are observed. Overall, the RTCP-FFT model successfully predicts the general trends observed in the measured ODF sections for the different strain paths considered in this study.

It should be mentioned that, Hu et al. (2012) presented results where the well-known crystal plasticity models such as VPSC and Taylor-type approximations tend to over predict the texture evolution for AA5754 due lack of proper treatment of grain to grain interaction and strain partitioning. On the other hand, the results in this research indicate that the RTCP-FFT model can accurately capture the trends of texture evolution due to consideration of the actual interaction of grains and allowing voxels in a grain to deform independently. This leads to an increase in distribution of orientations inside a grain, thus the substantial changes in texture are hindered, which lead to a more realistic texture evolution.

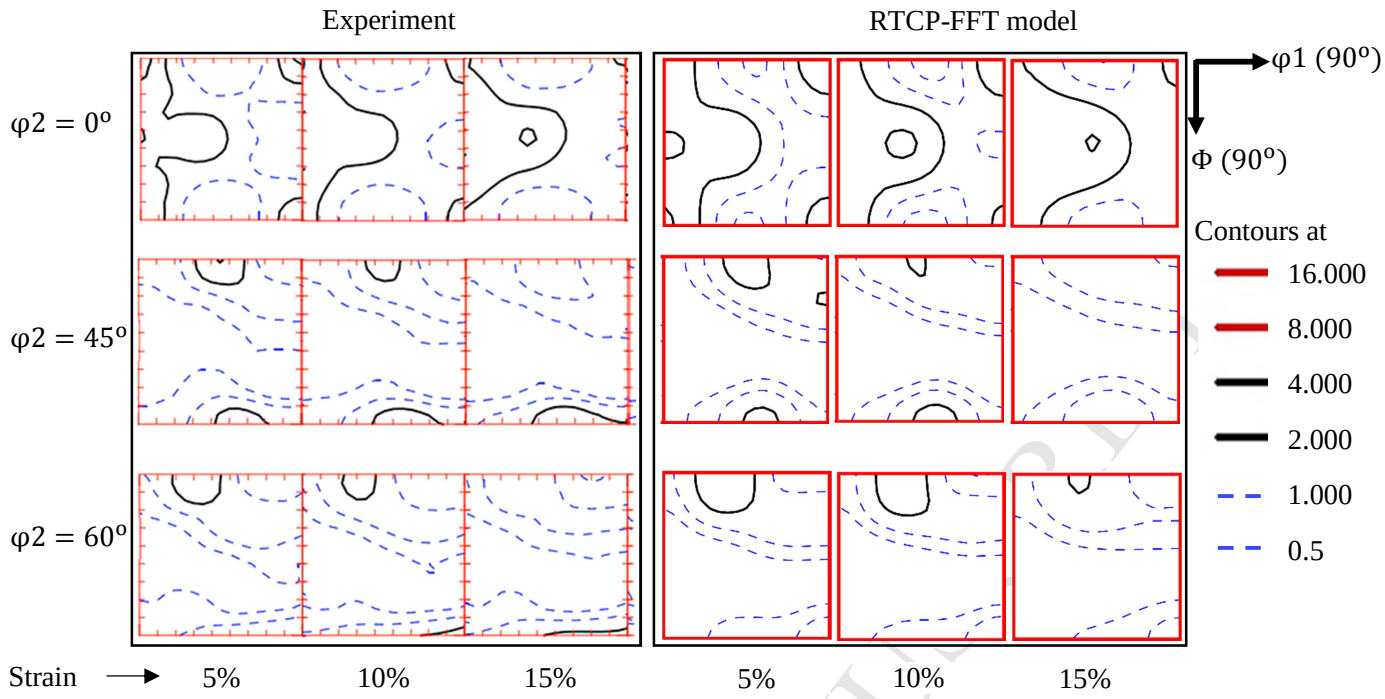

Fig. 10. Comparison of measured (Hu et al., 2011) and predicted ODF sections at strain levels of 5, 10, and 15 percent for equibiaxial tension.

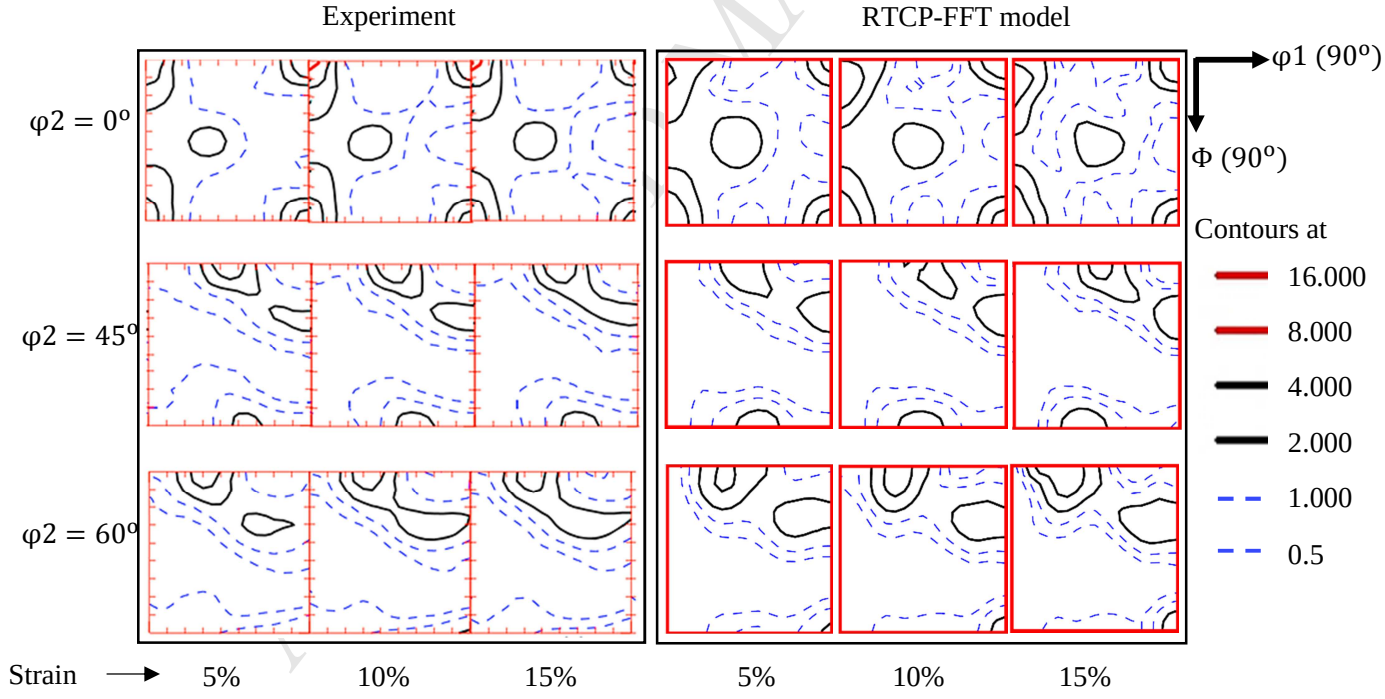

Fig. 11. Comparison of measured (Hu et al., 2011) and predicted ODF sections at strain levels of 5, 10, and 15 percent for plane strain tension in RD.

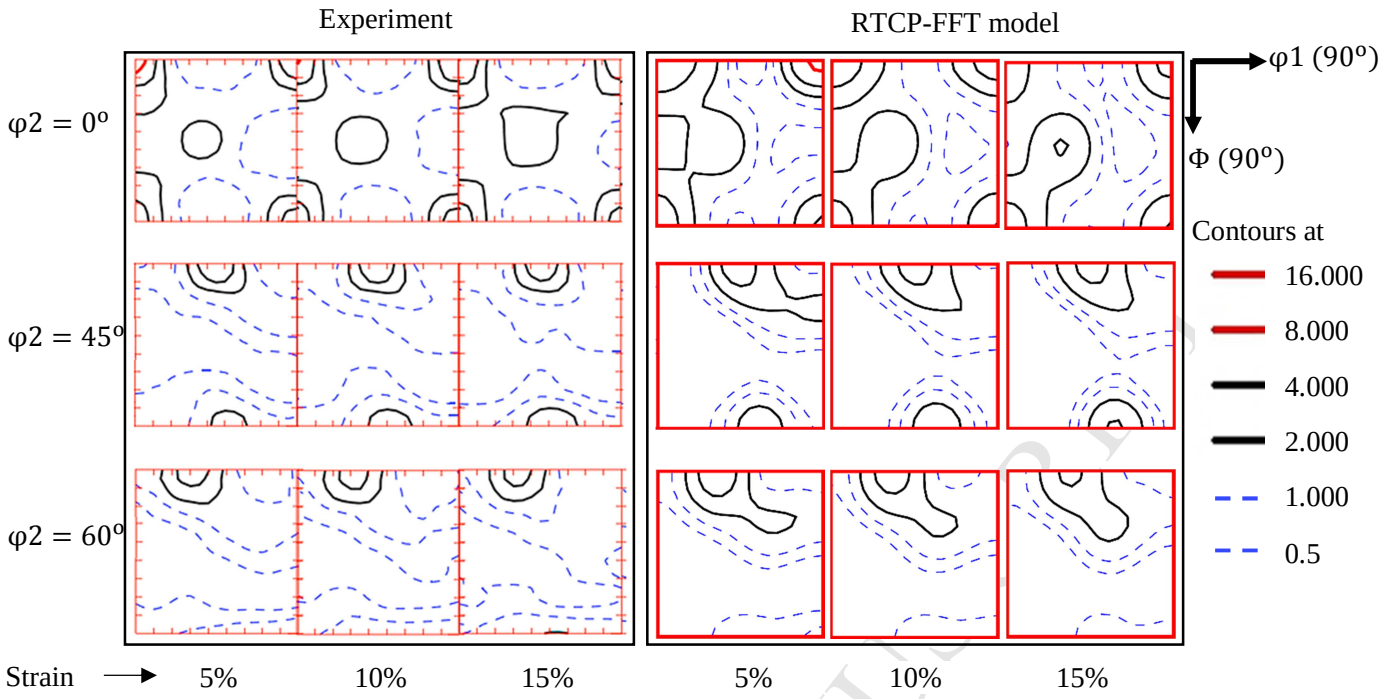

Fig. 12. Comparison of measured (Hu et al., 2011) and predicted ODF sections at strain levels of 5, 10, and 15 percent for plane strain tension in TD.

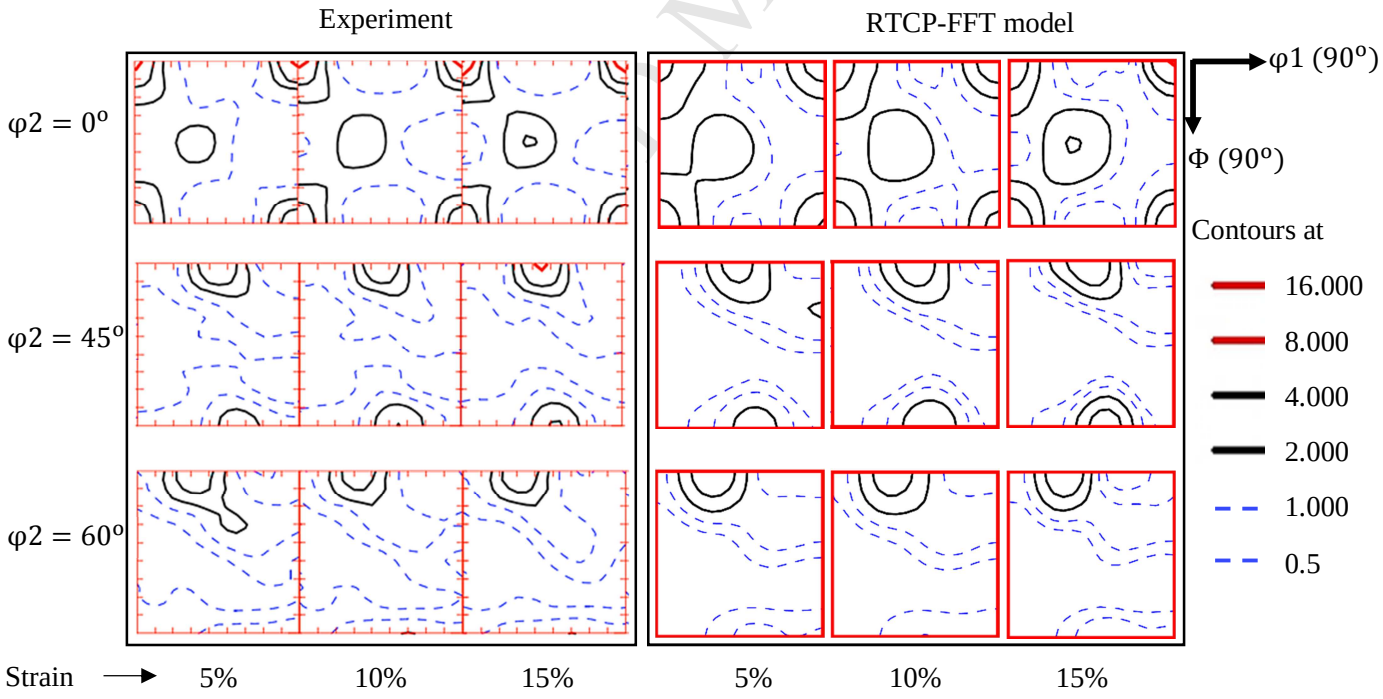

Fig. 13. Comparison of measured (Hu et al., 2011) and predicted ODF sections at strain levels of 5, 10, and 15 percent for uniaxial tension in TD.

4.6 Computational efficiency

Previous researches have demonstrated that the augmented Lagrangians scheme based FFT models are several orders more efficient than FEM based model in computing polycrystalline response under similar loading conditions (Liu et al., 2010; Prakash and Lebensohn, 2009). In present work, the EVP-FFT model is significantly modified to exploit its use in potential applications based on single-phase polycrystal modeling by further accelerating the FFT scheme using a semi-explicit rate tangent modulus method. In this section, a comparison of computational efficiency, in terms of CPU time, between the proposed RTCP-FFT model and the EVP-FFT model is presented using two different cases up to 20% true strain with a strain rate of 10^{-4} s^{-1}. The simulations were performed on a single processor of Intel(R) Xeon(R) CPU E5-2680 @ 2.70GHz at the University of Waterloo supercomputing centre without using any parallelization schemes.

In first case, for AA5754, the effect of different strain paths on CPU time is studied using a 16 x 16 x 16 regular grid of Fourier points in an RVE with 4096 Cube grains (Fig. 14a) corresponding to a single Fourier point per grain to minimize the number of calculations required for single temporal increment. Both RTCP-FFT and EVP-FFT models were first calibrated with uniaxial tension stress-strain curve along RD and then simulations were performed for plane strain tension along RD and balanced biaxial tension.

(a) Synthetic microstructure (b) CPU time comparison

Fig. 14. (a) The synthesized microstructure of AA5754 consisting of one Fourier point per grain with 16 Fourier points in each of x, y and z-axis representing 4096 Cube grains, the colors represent different grains. (b) Computational cost comparison of proposed model (RTCP-FFT) and EVP-FFT model for three different strain paths up to 20% true strain

The computation times for the RTCP-FFT and the EVP-FFT simulations for three different strain paths up to 20% true strain are summarized in Fig.14b. The EVP-FFT model required an average CPU time

of 19.39 minutes to simulate the material response for the three strain paths, while the RTCP-FFT model required an average CPU time of only 9.48 seconds. Thus, for the average CPU times, the RTCP-FFT model is 122.7 times faster than the EVP-FFT model. To further investigate the computational costs of the RTCP-FFT and the EVP-FFT models, the simulations of uniaxial tension with no strain hardening are also performed. The analysis shows that the RTCP-FFT model is 83 times faster than the EVP-FFT model when no strain hardening is considered.

In the second case, the effect of increasing the number of Fourier points per grain on the total CPU time is analyzed. For this case, six different RVEs are used; each consisting of 64 grains with 4 grains in X, Y and Z directions. The orientations of these grains are sampled from the AA5754 texture. Each RVE is then discretized using a regular Fourier grid of; a) 4 x 4 x 4 = 64 points, b) 8 x 8 x 8 = 512 points, c) 16 x 16 x 16 = 4096 points, d) 32 x 32 x 32 = 32768 points, e) 64 x 64 x 64 = 262144, and f) 128 x 128 x 128 = 2097152 points, respectively. Note that, the above mentioned discretization results in an increase in the number of Fourier points in each grain, with 1 x 1 x 1 = 1, 2 x 2 x 2 = 8, 4 x 4 x 4 = 64, 8 x 8 x 8 = 512, 16 x 16 x 16 = 4096, 32 x 32 x 32 = 32768 Fourier points per grain in RVEs described in a-e respectively. The RVEs are then subjected to uniaxial tension along RD (up to 20% true strain) with both models.

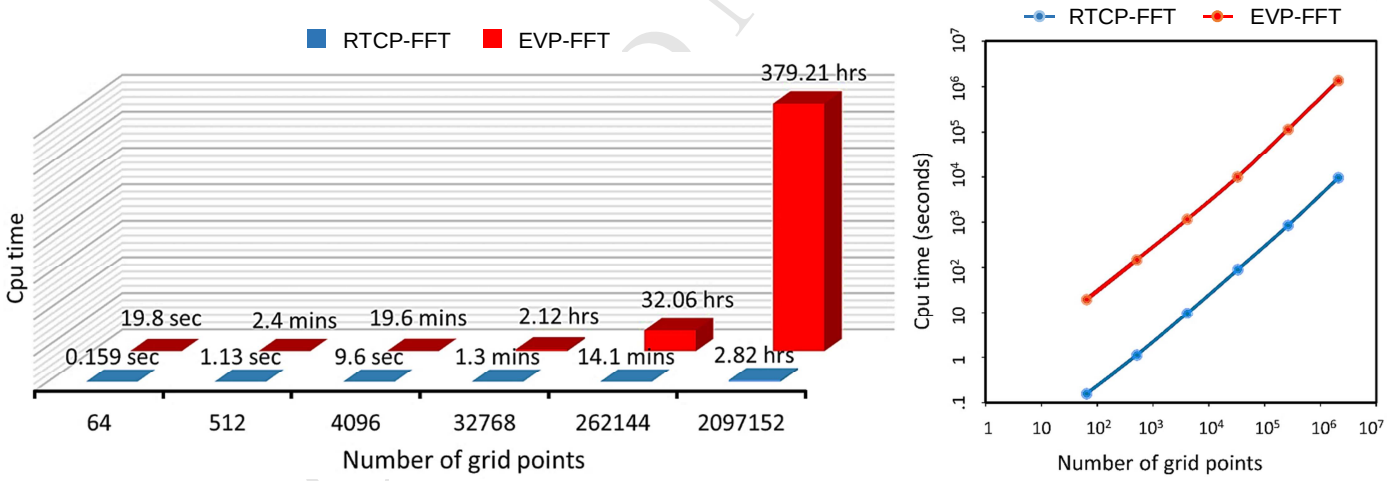

Fig. 15. A comparison of CPU time required by proposed model (RTCP-FFT) and EVP-FFT model respectively to complete RD uniaxial tension simulation up to 20% true strain versus total number of Fourier points in each of six different RVEs used; (a) Bar chart representation (b) log plot showing proportional limit

A comparison between the CPU times required by the two models to compute the response of six different RVEs with an applied strain rate of 10^{-4} s^{-1} is presented in Fig.15a. For each case, the RTCP-FFT model is, at an average, 110 times faster than EVP-FFT. Note that the computation times of the

simulations performed by both RTCP-FFT and EVP-FFT models scale proportionally with the number of Fourier points (Fig. 15b). This is a direct indication of the efficiency of both the models as both of the models employ an optimum matrix-inversion algorithm in the solver. The CPU times of the RTCP-FFT simulations are much quicker and fall about two orders of magnitude below that of the corresponding CPU times of the EVP-FFT simulations.

5. Summary and conclusions

A new, computationally efficient full-field numerical framework (RTCP-FFT) for single-phase polycrystalline solids is developed by coupling a tangent modulus method based crystal plasticity formulation with the fast Fourier transform (FFT) method to simulate large strain phenomena. The RTCP-FFT model is able to compute 3-D space-resolved local and overall micromechanical fields with high intragranular resolution using the direct input from images of microstructures of a polycrystalline material with extremely small computational cost.

The proposed numerical framework is verified by using simulations of the elastic-viscoplastic transitions of two polycrystals with the EVP-FFT model as a reference. As the first application with the RTCP-FFT model, for AA5754, the simulated stress-strain curves and texture evolution during five different strain paths are compared to experiments for model validation. Predictions with the RTCP-FFT model showed excellent agreement with experiments.

Simulations showed that the RTCP-FFT model is significantly faster than the EVP-FFT model in terms of CPU time; an acceleration of about two orders of magnitude is achieved over the augmented Lagrangians procedure based FFT methods. The solutions produced by the RTCP-FFT model can be slightly different locally (per material point) from those produced by the EVP-FFT model, however, these local variations (due to the difference in the integration algorithms) have with very little/no effect on macroscopic response.

Finally, the computational efficiency of the proposed numerical model makes it an excellent candidate to study the formability of polycrystalline metals since it can account for the richness of three-dimensional microstructures. Research with the proposed model to study the effect of various microstructural features (i.e., grain morphologies) on the forming limit strains is in progress and will be reported somewhere else.

Acknowledgements

The authors would like to acknowledge the financial support provided by the Natural Sciences and Engineering Research Council of Canada (NSERC). The authors, JSN, APB and KI, would like to thank Dr. Raja K. Mishra, GM R&D, for helpful discussions and making the measured experimental data on AA5754 available for this work. The authors would also like to acknowledge the center for high performance computing in Sherbrooke (RQHCP) for computational resources.

References

Abdolvand, H., Majkut, M., Oddershede, J., Schmidt, S., Lienert, U., Diak, B.J., Withers, P.J., Daymond, M.R., 2015. On the deformation twinning of Mg AZ31B: A three-dimensional synchrotron X-ray diffraction experiment and crystal plasticity finite element model. Int. J. Plast. 70, 77–97. doi:10.1016/j.ijplas.2015.03.001

Anglin, B.S., Lebensohn, R.A., Rollett, A.D., 2014. Validation of a numerical method based on Fast Fourier Transforms for heterogeneous thermoelastic materials by comparison with analytical solutions. Comput. Mater. Sci. 87, 209–217. doi:10.1016/j.commatsci.2014.02.027

Armstrong, R.W., Walley, S.M., 2008. High strain rate properties of metals and alloys. Int. Mater. Rev. 53, 105–128. doi:10.1179/174328008X277795

Asaro, R.J., Needleman, A., 1985. Overview no. 42 Texture development and strain hardening in rate dependent polycrystals. Acta Metall. 33, 923–953. doi:10.1016/0001-6160(85)90188-9

Brahme, A., Alvi, M.H., Saylor, D., Fridy, J., Rollett, A.D., 2006. 3D reconstruction of microstructure in a commercial purity aluminum. Scr. Mater. 55, 75–80. doi:10.1016/j.scriptamat.2006.02.017

Brahme, A.P., Inal, K., Mishra, R.K., Saimoto, S., 2011. A new strain hardening model for rate-dependent crystal plasticity. Comput. Mater. Sci. 50, 2898–2908. doi:10.1016/j.commatsci.2011.05.006

Brenner, R., Lebensohn, R.A., Castelnau, O., 2009. Elastic anisotropy and yield surface estimates of polycrystals. Int. J. Solids Struct. 46, 3018–3026.

Chang, Y.W., Asaro, R.J., 1981. An experimental study of shear localization in aluminum-copper single crystals. Acta Metall. 29, 241–257. doi:10.1016/0001-6160(81)90103-6

Cyr, E.D., Mohammadi, M., Mishra, R.K., Inal, K., 2015. A three dimensional (3D) thermo-elasto-viscoplastic constitutive model for FCC polycrystals. Int. J. Plast. 70, 166–190. doi:10.1016/j.ijplas.2015.04.001

de Geus, T.W.J., Vond??ejc, J., Zeman, J., Peerlings, R.H.J., Geers, M.G.D., 2017. Finite strain FFT-based non-linear solvers made simple. Comput. Methods Appl. Mech. Eng. 318, 412–430. doi:10.1016/j.cma.2016.12.032

Eisenlohr, P., Diehl, M., Lebensohn, R.A., Roters, F., 2013. A spectral method solution to crystal elasto-viscoplasticity at finite strains. Int. J. Plast. 46, 37–53. doi:10.1016/j.ijplas.2012.09.012

Erinosho, T.O., Collins, D.M., Wilkinson, A.J., Todd, R.I., Dunne, F.P.E., 2016. Assessment of X-ray diffraction and crystal plasticity lattice strain evolutions under biaxial loading. Int. J. Plast. 83, 1–18. doi:10.1016/j.ijplas.2016.03.011

Gardner, C.J., Adams, B.L., Basinger, J., Fullwood, D.T., 2010. EBSD-based continuum dislocation microscopy. Int. J. Plast. 26, 1234–1247. doi:10.1016/j.ijplas.2010.05.008

Grennerat, F., Montagnat, M., Castelnau, O., Vacher, P., Moulinec, H., Suquet, P., Duval, P., 2012. Experimental characterization of the intragranular strain field in columnar ice during transient creep. Acta Mater. 60, 3655–3666. doi:10.1016/j.actamat.2012.03.025

Hu, L., Rollett, A.D., Iadicola, M., Foecke, T., Banovic, S., 2012. Constitutive relations for AA 5754 based on crystal plasticity. Metall. Mater. Trans. A Phys. Metall. Mater. Sci. 43, 854–869. doi:10.1007/s11661-011-0927-1

Inal, K., Mishra, R.K., 2012. Crystal plasticity based numerical modelling of large strain deformation in hexagonal closed packed metals, in: Procedia IUTAM. pp. 239–273. doi:10.1016/j.piutam.2012.03.016

Inal, K., Mishra, R.K., Cazacu, O., 2010. Forming simulation of aluminum sheets using an anisotropic yield function coupled with crystal plasticity theory. Int. J. Solids Struct. 47, 2223–2233. doi:10.1016/j.ijsolstr.2010.04.017

Inal, K., Neale, K.W., Wu, P.D., 2002a. Parallel finite element algorithms for the analysis of multiscale plasticity problems, Advances in High Performance Computing (Vol. 7).

Inal, K., Wu, P.D., Neale, K.W., 2002b. Finite element analysis of localization in FCC polycrystalline sheets under plane stress tension 39, 3469–3486.

Izadbakhsh, A., Inal, K., Mishra, R.K., Niewczas, M., 2011. New crystal plasticity constitutive model for large strain deformation in single crystals of magnesium. Comput. Mater. Sci. 50, 2185–2202. doi:10.1016/j.commatsci.2011.02.030

Jeong, Y., Gnäupel-Herold, T., Barlat, F., Iadicola, M., Creuziger, A., Lee, M.-G., 2015. Evaluation of

biaxial flow stress based on elasto-viscoplastic self-consistent analysis of X-ray diffraction measurements. Int. J. Plast. 66, 103–118. doi:10.1016/j.ijplas.2014.06.009

Kabel, M., Fliegener, S., Schneider, M., 2016. Mixed boundary conditions for FFT-based homogenization at finite strains. Comput. Mech. 57, 193–210. doi:10.1007/s00466-015-1227-1

Kalidindi, S.R., Bronkhorst, C.A., Anand, L., 1992. Crystallographic texture evolution in bulk deformation processing of FCC metals. J. Mech. Phys. Solids 40, 537–569. doi:10.1016/0022-5096(92)80003-9

Karel, J., Casoli, F., Lupo, P., Nasi, L., Fabbrici, S., Righi, L., Albertini, F., Felser, C., 2016. Evidence for in-plane tetragonal c-axis in MnxGa1–x thin films using transmission electron microscopy. Scr. Mater. 114, 165–169. doi:10.1016/j.scriptamat.2015.11.019

Lebensohn, R.A., 2001. N-site modeling of a 3D viscoplastic polycrystal using Fast Fourier Transform. Acta Mater. 49, 2723–2737. doi:10.1016/S1359-6454(01)00172-0

Lebensohn, R.A., Brenner, R., Castelnau, O., Rollett, A.D., 2008. Orientation image-based micromechanical modelling of subgrain texture evolution in polycrystalline copper. Acta Mater. 56, 3914–3926. doi:10.1016/j.actamat.2008.04.016

Lebensohn, R.A., Kanjarla, A.K., Eisenlohr, P., 2012. An elasto-viscoplastic formulation based on fast Fourier transforms for the prediction of micromechanical fields in polycrystalline materials. Int. J. Plast. 32–33, 59–69. doi:10.1016/j.ijplas.2011.12.005

Lebensohn, R.A., Rollett, A.D., Suquet, P., 2011. Keeping up with emerging characterization methods of crystalline materials: Fast Fourier Transform-based modelling for the determination of micromechanical fields in polycrystals Ricardo A. Lebensohn, Anthony D. Rollett and Pierre Suquet 3, 13–18.

Lebensohn, R.A., Tomé, C.N., 1993. A self-consistent anisotropic approach for the simulation of plastic deformation and texture development of polycrystals: Application to zirconium alloys. Acta Metall. Mater. 41, 2611–2624. doi:10.1016/0956-7151(93)90130-K

Lebensohn, R.A., Tomé, C.N., CastaÑeda, P.P., 2007. Self-consistent modelling of the mechanical behaviour of viscoplastic polycrystals incorporating intragranular field fluctuations. Philos. Mag. 87, 4287–4322. doi:10.1080/14786430701432619

Lee, E.H., 1969. Elastic-Plastic Deformation at Finite Strains. J. Appl. Mech. 36, 1. doi:10.1115/1.3564580

Lee, W.-S., Lam, H.-F., 1996. The deformation behaviour and microstructure evolution of high-strength alloy steel at high rate of strain. J. Mater. Process. Technol. 57, 233–240. doi:10.1016/0924-0136(95)02068-3

Lippmann, B.A., Schwinger, J., 1950. Variational Principles for Scattering Processes. Phys. Rev. 79, 469–480.

Liu, B., Raabe, D., Roters, F., Eisenlohr, P., Lebensohn, R. a, 2010. Comparison of finite element and fast Fourier transform crystal plasticity solvers for texture prediction. Model. Simul. Mater. Sci. Eng. 18, 85005. doi:10.1088/0965-0393/18/8/085005

Michel, J.C., Moulinec, H., Suquet, P., 2001. A computational scheme for linear and non-linear composites with arbitrary phase contrast. 5th U.S. Natl. Congr. Comput. Mech. 4-6 Aug. 1999 52, 139–160. doi:10.1002/nme.275

Molinari, A., Canova, G.R., Ahzi, S., 1987. A self consistent approach of the large deformation polycrystal viscoplasticity. Acta Metall. 35, 2983–2994. doi:10.1016/0001-6160(87)90297-5

Moulinec, H., Suquet, P., 1998. A numerical method for computing the overall response of nonlinear composites with complex microstructure. Comput. Methods Appl. Mech. Eng. 157, 69–94. doi:10.1016/S0045-7825(97)00218-1

Moulinec, H., Suquet, P., 1994. A fast numerical method for computing the linear and nonlinear mechanical properties of composites. Comptes Rendus l'Academie des Sci. Ser. II 318, 1417–1423.

Muhammad, W., Mohammadi, M., Kang, J., Mishra, R.K., Inal, K., 2015. An elasto-plastic constitutive model for evolving asymmetric/anisotropic hardening behavior of AZ31B and ZEK100 magnesium alloy sheets considering monotonic and reverse loading paths. Int. J. Plast. 70, 30–59. doi:10.1016/j.ijplas.2015.03.004

Nemat-Nasser, S., Ni, L., Okinaka, T., 1998. A constitutive model for fcc crystals with application to polycrystalline OFHC copper. Mech. Mater. 30, 325–341. doi:10.1016/S0167-6636(98)00055-6

Nieh, T.G., Hsiung, L.M., Wadsworth, J., Kaibyshev, R., 1998. High strain rate superplasticity in a continuously recrystallized Al–6%Mg–0.3%Sc alloy. Acta Mater. 46, 2789–2800. doi:10.1016/S1359-6454(97)00452-7

Ohashi, T., Barabash, R.I., Pang, J.W.L., Ice, G.E., Barabash, O.M., 2009. X-ray microdiffraction and strain gradient crystal plasticity studies of geometrically necessary dislocations near a Ni bicrystal grain boundary. Int. J. Plast. 25, 920–941. doi:10.1016/j.ijplas.2008.04.009

Peirce, D., Asaro, R.J., Needleman, A., Park, A., 1983. Overview Material Rate Dependence and Localized Deformation in Crystalline Solids 31, 1951–1976.

Pinna, C., Lan, Y., Kiu, M.F., Efthymiadis, P., Lopez-pedrosa, M., 2015. Assessment of crystal plasticity fi nite element simulations of the hot deformation of metals from local strain and orientation measurements. Int. J. Plast. 73, 24–38. doi:10.1016/j.ijplas.2015.05.015

Prakash, a, Lebensohn, R. a, 2009. Simulation of micromechanical behavior of polycrystals: finite elements versus fast Fourier transforms. Model. Simul. Mater. Sci. Eng. 17, 64010. doi:10.1088/0965-0393/17/6/064010

Rashid, M.M., Nemat-Nasser, S., 1992. A constitutive algorithm for rate-dependent crystal plasticity. Comput. Methods Appl. Mech. Eng. 94, 201–228. doi:10.1016/0045-7825(92)90147-C

Rossiter, J., Brahme, A., Simha, M.H., Inal, K., Mishra, R., 2010. A new crystal plasticity scheme for explicit time integration codes to simulate deformation in 3D microstructures: Effects of strain path, strain rate and thermal softening on localized deformation in the aluminum alloy 5754 during simple shear. Int. J. Plast. 26, 1702–1725. doi:10.1016/j.ijplas.2010.02.007

Salem, A.A., Kalidindi, S.R., Doherty, R.D., 2003. Strain hardening of titanium: role of deformation twinning. Acta Mater. 51, 4225–4237. doi:10.1016/S1359-6454(03)00239-8

Spowart, J.E., Mullens, H.E., Puchala, B.T., 2003. Collecting and analyzing microstructures in three dimensions: A fully automated approach. JOM 55, 35–37. doi:10.1007/s11837-003-0173-0

Taylor, G.I., 1938. Plastic strain in metals. J. Inst. Met. 62, 307–324.

Wickramarachchi, S.J., Ikeda, T., Dassanayake, B.S., Keerthisinghe, D., Tanis, J.A., 2016. Incident energy and charge deposition dependences of electron transmission through a microsized tapered glass capillary. Nucl. Instruments Methods Phys. Res. Sect. B Beam Interact. with Mater. Atoms. doi:10.1016/j.nimb.2016.06.006

Highlights:

- Efficient full field elasto-viscoplastic framework that gives a speedup of ~100
- Framework combines rate tangent method and Fast Fourier Transform
- Extending the EVP-FFT model to simulate large strain behavior
- Accurate predictions of different strain paths using calibrated uniaxial tension